Increasing stability and accuracy of the lattice Boltzmann scheme: recursivity and regularization

Orestis Malaspinas*[a,b]

[a]Institut Jean le Rond d'Alembert, UMR 7190, Université Pierre et Marie Curie - Paris 6, 4 place Jussieu - case 162, F-75252, France
[b]Centre Universitaire d'Informatique, Université de Genève 7, route de Drize, CH-1227 Switzerland

May 27, 2015

Abstract

In the present paper a lattice Boltzmann scheme is presented which exhibits an increased stability and accuracy with respect to standard single- or multi-relaxa-tion-time (MRT) approaches. The scheme is based on a single-relaxation-time model where a special regularization procedure is applied. This regularization is based on the fact that, for a-thermal flows, there exists a recursive way to express the velocity distribution function at any order (in the Hermite series sense) in terms of the density, velocity, and stress tensor. A linear stability analysis is conducted which shows enhanced dispersion/dissipation relations with respect to existing models. The model is then validated on two (one 2D and one 3D) moderately high Reynolds number simulations (Re $\sim$ 1000) at moderate Mach numbers (Ma $\sim$ 0.5). In both cases the results are compared with an MRT model and an enhanced accuracy and stability is shown by the present model.

1 Introduction

The lattice Boltzmann method (LBM) is a widely used tool for numerical simulations of fluid flows. It has become over the years one the of the major engineering tools for computational fluid mechanics. It describes the flow thanks to the time evolution of the velocity distribution function which is only modified through the effect of inter-particle collisions.

The most commonly used lattice Boltzmann collision model is the single relaxation time model or BGK (for Bhathagar, Gross and Krook, see Bhatnagar et al. [1954]). This model is able to asymptotically represent weakly compressible fluids (through a Chapman–Enskog expansion, see Chapman and Cowling [1960]). Nevertheless it suffers from stability issues especially at high Reynolds numbers. These issues are due to the "ghost-modes" (see Dellar [2001] for a discussion) which are non-physical moments present in any LBM simulation in

*orestis.malaspinas@unige.ch

excess of the density (pressure), velocity and stress. This issue has been addressed by several authors and several solutions have been proposed. The first is the multiple-relaxation-time (MRT) approach (see d'Humières [1992], Lallemand and Luo [2000], d'Humières et al. [2002], Dellar [2001], Xu and Sagaut [2011], Xu et al. [2012] among others) which uses a more complex collision model involving several relaxation times adjusted with the help of a linear stability analysis in order to optimize their dispersion/dissipation relations. The entropic approach ensures the positivity of the distribution functions and hence the unconditional stability by adding an H-theorem to the BGK model. The effect of the H-theorem is essentially to increase locally the viscous dissipation of the model (see Ansumali and Karlin [2002], Boghosian et al. [2003], Chikatamarla et al. [2006], Malaspinas et al. [2008] among others). The regularization approach (see Latt and Chopard [2006], Zhang et al. [2006]) which can be interpreted as a subclass of MRT methods where the "ghost-modes" are relaxed towards zero with characteristic time 1. Finally the selective viscosity models proposed by Ricot et al. [2009] use non-local low-pass filters to remove high frequency oscillations (which are responsible for the numerical instabilities) in order to increase the stability.

In this paper we will first show a recursive way to compute the moments of the distribution function as long as the Chapman–Enskog expansion is valid (low Knudsen number) for the BGK collision operator. This recursive relation will then be used to "regularize" the distribution function and provide a very stable and accurate scheme even at moderately high Reynolds numbers and (relatively) high Mach numbers (smaller than one though). We also show that the present model is more accurate and more stable than the existing MRT methods by performing a linear stability analysis and several numerical benchmarks.

The paper is structured as follows. In Sec. 2 a reminder of fundamentals for fluid flows with the Boltzmann–BGK equation is presented. Then in Sec. 3 the new model is proposed and analyzed. It is validated in Sec. 4 on a 2D and a 3D benchmark. Finally the present work is concluded in Sec. 5 and perspectives are given.

2 The hydrodynamic limit of the BGK equation

The following section aims at introducing the basic notations as well as showing the fundamentals of the expansion leading from the continuous Boltzmann-BGK equation to the Navier–Stokes equations. More details can be found in Shan et al. [2006] and Malaspinas [2009] for example.

The Boltzmann equation describes the time evolution of the velocity density probability distribution $f(\boldsymbol{x}, \boldsymbol{\xi}, t)$ of finding a particle with velocity $\boldsymbol{\xi}$ at position $\boldsymbol{x}$ and time t in terms of particle collisions only, and reads in absence of a force as

$$\partial_t f(\boldsymbol{x}, \boldsymbol{\xi}, t) + (\boldsymbol{\xi} \cdot \boldsymbol{\nabla}) f(\boldsymbol{x}, \boldsymbol{\xi}, t) = \Omega(f), \tag{1}$$

where Ω is the collision operator. Assuming also that the fluid is athermal (absence of temperature), the macroscopic fields of interest, the density ρ, the velocity $\boldsymbol{u}$, and the stress tensor $\boldsymbol{P}$ are given by the following moments of the

distribution function

$$\rho = \int \mathrm{d}\boldsymbol{\xi}\ f(\boldsymbol{x}, \boldsymbol{\xi}, t), \tag{2}$$

$$\rho \boldsymbol{u} = \int \mathrm{d}\boldsymbol{\xi}\ \boldsymbol{\xi} f(\boldsymbol{x}, \boldsymbol{\xi}, t), \tag{3}$$

$$\boldsymbol{P} = \int \mathrm{d}\boldsymbol{c}\ \boldsymbol{cc} f(\boldsymbol{x}, \boldsymbol{\xi}, t), \tag{4}$$

where $\boldsymbol{c} = \boldsymbol{\xi} - \boldsymbol{u}$ is the microscopic velocity in the co-moving frame and $\boldsymbol{cc}$ denotes the tensor product of $\boldsymbol{c}$ with itself.

The most widely used model for computational fluid dynamics for the collision operator is the BGK, single relaxation time approximation, in which the Boltzmann equation reads

$$\partial_t f(\boldsymbol{x}, \boldsymbol{\xi}, t) + (\boldsymbol{\xi} \cdot \boldsymbol{\nabla}) f(\boldsymbol{x}, \boldsymbol{\xi}, t) = -\frac{1}{\tau} \left(f(\boldsymbol{x}, \boldsymbol{\xi}, t) - f^{(0)}(\rho, \boldsymbol{u}) \right), \tag{5}$$

where τ the relaxation time, and $f^{(0)}$ is the local Maxwell–Boltzmann equilibrium distribution function, which in non-dimensional units is given by

$$f^{(0)} = \frac{\rho(\boldsymbol{x}, t)}{(2\pi)^{D/2}} \exp\left(-\frac{(\boldsymbol{u}(\boldsymbol{x}, t) - \boldsymbol{\xi})^2}{2} \right), \tag{6}$$

D being the physical dimension.

Since we are interested in numerically solving Eq. (5) in an efficient fashion that nevertheless represents accurately fluid flows, certain simplifications will be made. In particular instead of considering the complete form of the Maxwell–Boltzmann distribution function, only a polynomial approximation will be used.

Following an idea by Shan et al. [2006] (or Grad [1949b] for the original use of this expansion in the frame of the Boltzmann equation), one can expand the distribution functions f and $f^{(0)}$, in Hermite polynomials up to an arbitrary order N (see Grad [1949a] for a summary on Hermite polynomials)

$$f^N = w(\boldsymbol{\xi}) \sum_{n=0}^{N} \frac{1}{n!} \mathcal{H}^{(n)}(\boldsymbol{\xi}) : \boldsymbol{a}^{(n)}, \quad {f^{(0)}}^N = w(\boldsymbol{\xi}) \sum_{n=0}^{N} \frac{1}{n!} \mathcal{H}^{(n)}(\boldsymbol{\xi}) : \boldsymbol{a}_0^{(n)}, \tag{7}$$

where the colon symbol ":" stands for the full index contraction. The Hermite polynomials of order n and the associated Gaussian weight are noted $\mathcal{H}^{(n)}$ and $w(\boldsymbol{\xi}) = \exp(-\boldsymbol{\xi}^2/2)$ respectively. The Hermite coefficients of f and $f^{(0)}$ of degree n are respectively given by $\boldsymbol{a}^{(n)}$ and $\boldsymbol{a}_0^{(n)}$. From now on, we will always omit the superscript N and assume that the distribution function (and its equilibrium counterpart) is represented by its approximate form in terms of Hermite polynomials up to an arbitrary order N except when explicitly stated otherwise. The equilibrium coefficients can be easily computed and are found to be up to order three

$$a_0^{(0)} = \rho, \tag{8}$$

$$a_{0\alpha}^{(1)} = \rho u_\alpha, \tag{9}$$

$$a_{0\alpha\beta}^{(2)} = \rho u_\alpha u_\beta, \tag{10}$$

$$a_{0\alpha\beta\gamma}^{(3)} = \rho u_\alpha u_\beta u_\gamma. \tag{11}$$

In order to recover the macroscopic equations of motion related with the BGK equation, one must take moments of Eq. (5). By taking the moments related with density (order zero) and momentum (order one) of this equation, one gets after some algebra and the use of Eqs. (2)-(4) and (8)-(10)

$$\partial_t \rho + \boldsymbol{\nabla} \cdot (\rho \boldsymbol{u}) = 0, \tag{12}$$

$$\partial_t (\rho \boldsymbol{u}) + \boldsymbol{\nabla} \cdot (\rho \boldsymbol{u}\boldsymbol{u}) + \boldsymbol{\nabla} \cdot \boldsymbol{P} = 0. \tag{13}$$

These equations are obtained under the sole assumption of mass and momentum conservation ($\int \Omega = \int \boldsymbol{\xi}\Omega = 0$), or in other terms

$$\int \mathrm{d}\boldsymbol{\xi}\ (f - f^{(0)}) = 0, \qquad \text{Mass conservation} \tag{14}$$

$$\int \mathrm{d}\boldsymbol{\xi}\ \boldsymbol{\xi}(f - f^{(0)}) = 0, \qquad \text{Momentum conservation} \tag{15}$$

The momentum conservation equation still needs to be closed (a constitutive equation must be found for $\boldsymbol{P}$). In order to do so, one can use the Chapman–Enskog expansion (see Chapman and Cowling [1960], Huang [1987]). Since the expansion in Hermite series is used for discretization purposes we will discuss the Chapman–Enskog expansion in this frame (although the Hermite series is not a prerequisite for performing the Chapman–Enskog expansion).

The Chapman–Enskog expansion is based on the assumption that the distribution function f is given by the sum of the equilibrium distribution, $f^{(0)}$, plus a small perturbation noted $f^{(1)}$,

$$f = f^{(0)} + f^{(1)}, \tag{16}$$

where the equilibrium distribution is assumed to be given by Eq. (7). The perturbation, $f^{(1)} \sim \emptyset(Kn) \ll f^{(0)}$, is of the order of the Knudsen number, Kn. As for f and $f^{(0)}$ one can express $f^{(1)}$ in terms of a Hermite series

$$f^{(1)} = w(\boldsymbol{\xi}) \sum_{n=0}^{N} \frac{1}{n!} \mathcal{H}^{(n)}(\boldsymbol{\xi}) : \boldsymbol{a}_1^{(n)}, \tag{17}$$

where $\boldsymbol{a}_1^{(n)}$ is the Hermite coefficient of $f^{(1)}$ at order n. The derivation which is presented hereafter is not the standard one found in the literature and rather follows Huang [1987].

Replacing the Chapman–Enskog Ansatz in Eq. (5), one obtains at the lowest order

$$\partial_t f^{(0)} + (\boldsymbol{\xi} \cdot \boldsymbol{\nabla}) f^{(0)} = -\frac{1}{\tau} f^{(1)}. \tag{18}$$

Taking the zeroth and first order moments of this equation and using the mass and momentum conservation constrains on each equation respectively ($\int f^{(1)} = \int \boldsymbol{\xi} f^{(1)} = 0$), one gets the inviscid Euler equations for mass, momentum and energy conservation

$$\partial_t \rho + \boldsymbol{\nabla} \cdot (\rho \boldsymbol{u}) = 0, \tag{19}$$

$$\partial_t (\rho \boldsymbol{u}) + \boldsymbol{\nabla} \cdot (\rho \boldsymbol{u}\boldsymbol{u}) + \boldsymbol{\nabla} p = 0, \tag{20}$$

where $p = \rho$ is the perfect gas law (remember that there is no temperature).

The stress tensor can be decomposed in its Chapman–Enskog counterparts

$$\boldsymbol{P} = \boldsymbol{P}^{(0)} + \boldsymbol{P}^{(1)} = \rho \boldsymbol{I} + \boldsymbol{P}^{(1)}, \tag{21}$$

where $\boldsymbol{P}^{(j)} = \int \boldsymbol{cc} f^{(j)}$ for $j = 0, 1$ (j corresponding to the Chapman–Enskog index). Thus we are left with the computation of $\boldsymbol{P}^{(1)}$ which for simplicity is computed through the Hermite expansion of the distribution function. Let us define $\boldsymbol{a}_1^{(n)}$ the Hermite coefficient of order n of the off-equilibrium distribution function $f^{(1)}$ and express $\boldsymbol{P}^{(1)}$ in terms of these Hermite coefficients

$$P^{(1)}_{\alpha\beta} = a^{(2)}_{1\alpha\beta}, \tag{22}$$

where we used that by construction $\boldsymbol{a}_1^{(0)} = \boldsymbol{a}_1^{(1)} = 0$. Then projecting Eq. (18) on the Hermite basis, it follows that

$$\partial_t \boldsymbol{a}_0^{(n)} + \boldsymbol{\nabla} \cdot \boldsymbol{a}_0^{(n+1)} + \left(\boldsymbol{\nabla} \boldsymbol{a}_0^{(n-1)} + \text{perm} \right) = -\frac{1}{\tau} \boldsymbol{a}_1^{(n)}, \tag{23}$$

where "perm" stands for all the cyclic index permutations. For $n = 2$ this equation becomes

$$\begin{aligned} &\partial_t \boldsymbol{a}_0^{(2)} + \boldsymbol{\nabla} \cdot \boldsymbol{a}_0^{(3)} + \left(\boldsymbol{\nabla} \boldsymbol{a}_0^{(1)} + \text{perm} \right) = -\frac{1}{\tau} \boldsymbol{a}_1^{(2)}, \\ &\partial_t \left(\rho \boldsymbol{uu} \right) + \boldsymbol{\nabla} \cdot \left(\rho \boldsymbol{uuu} \right) + \left(\boldsymbol{\nabla} (\rho \boldsymbol{u}) + (\boldsymbol{\nabla} (\rho \boldsymbol{u}))^{\mathrm{T}} \right) = -\frac{1}{\tau} \boldsymbol{a}_1^{(2)}. \end{aligned} \tag{24}$$

By using Eqs. (19)-(20) to eliminate the time derivative terms, this equation can be rewritten (after some tedious algebra that can be found in Malaspinas [2009]) as

$$\boldsymbol{a}_1^{(2)} = \boldsymbol{P}^{(1)} = -2\tau\rho \boldsymbol{S}, \tag{25}$$

where

$$\boldsymbol{S} = \frac{1}{2} \left(\boldsymbol{\nabla u} + (\boldsymbol{\nabla u})^{\mathrm{T}} \right). \tag{26}$$

By comparing Eq. (25) with the Navier–Stokes equations, the transport coefficient μ can be identified with the relaxation time through the following relation

$$\mu = \rho\tau. \tag{27}$$

Finally the equations of motion obtained are the weakly compressible athermal Navier–Stokes equations

$$\partial_t \rho + \boldsymbol{\nabla} \cdot (\rho \boldsymbol{u}) = 0, \tag{28}$$

$$\partial_t (\rho \boldsymbol{u}) + \boldsymbol{\nabla} \cdot (\rho \boldsymbol{uu}) = -\boldsymbol{\nabla} p + \boldsymbol{\nabla} \cdot (2\mu \boldsymbol{S}). \tag{29}$$

3 Hierarchy of non-equilibrium moments and regularization scheme

In this section a novel theoretical approach is proposed for the athermal Boltzmann-BGK equation. A recursive formulation for non-equilibrium moments is shown to exist and a regularization technique is proposed for the discrete lattice Boltzmann method.

3.1 Recursive properties of high order moments

The particular structure of the moments of the equilibrium distribution in absence of temperature allows for an elegant formulation of the high order (higher than two) non-equilibrium moments.

The Hermite coefficients of order n of the equilibrium distribution can be recursively expressed as

$$\boldsymbol{a}_0^{(n)} = \boldsymbol{a}_0^{(n-1)}\boldsymbol{u}, \text{ and } a_0^{(0)} = \rho. \tag{30}$$

Using this relation and Eqs. (19)-(20) one can show that for $n \geq 3$ (see A for the proof)

$$a^{(n)}_{1,\alpha_1\ldots\alpha_n} = a^{(n-1)}_{1,\alpha_1\ldots\alpha_{n-1}} u_{\alpha_n} + \left(u_{\alpha_1}\ldots u_{\alpha_{n-2}} a^{(2)}_{1,\alpha_{n-1}\alpha_n} + \text{perm}(\alpha_n)\right), \tag{31}$$

where "perm(α_n)" stands for all the cyclic index permutations of indexes from α_1 to α_{n-1} (α_n is never permuted). One therefore notices that a Hermite coefficient of order n can be expressed in terms of the the velocity and the Hermite coefficients of order order two and $n-1$. This property allows to reconstruct the populations up to any order by only knowing its second order coefficient and the macroscopic velocity.

3.2 Discretization of the microscopic velocity space

We notice that only the Hermite coefficients of the distribution function are used in the Chapman–Enskog expansion. Therefore in order to asymptotically recover the Navier–Stokes equations there is no need to use the complete Maxwell–Boltzmann equilibrium distribution but only a polynomial expansion of it. In order to discretize the velocity space one will use a Gauss–Hermite quadrature. The aim of this discretization is to exactly evaluate the integral of polynomials of order m with Gaussian weight as a sum

$$\int \mathrm{d}\boldsymbol{\xi} w(\boldsymbol{\xi}) p_m(\boldsymbol{\xi}) = \sum_{i=0}^{q-1} w_i p_m(\boldsymbol{\xi}_i), \tag{32}$$

where $\{w_i\}_{i=0}^{q-1}$ and $\{\boldsymbol{\xi}_i\}_{i=0}^{q-1}$ are two sets of q constant weights and abscissae respectively.

In order to obtain asymptotically the weakly compressible limit of the BGK equation only polynomials of order $m = 5$ need to be integrated exactly. The associated most common quadratures (see Shan et al. [2006]) for this case are given by the D2Q9 (in 2D) and the D3Q15, D3Q19, and D3Q27 lattices[1] (in 3D). These quadratures allow the definition of a set of velocity discretized distribution function noted as $\{f_i\}_{i=0}^{q-1} \equiv \{f(\boldsymbol{x}, \boldsymbol{\xi}_i, t)\}_{i=0}^{q-1}$. In other terms, on each position $\boldsymbol{x}$ at time t one defines q independent values $\{f_i\}_{i=0}^{q-1}$. These quantities can therefore be represented on a q-dimensional basis (see work of d'Humières [1992], Dellar [2003] among others). We emphasize here is that there are two different spaces that must be distinguished: the velocity-discretized q-dimensional space and the d-dimensional physical space.

[1] The DdQq notation denotes a lattice of dimension d and with q quadrature points

The above quadratures only allow the exact representation of the populations up to second order in Hermite polynomials, one usually truncates Eq. (7) to order two. This means that the equilibrium distribution is represented on a six-dimensional basis in 2D and respectively on a 10-dimensional basis in 3D, while it is living in a 9 (for the D2Q9 lattice) or 15, 19, or 27 (for the D3Q15, D3Q19, or D3Q27 lattices) dimensional space (depending on the quadrature used).

The BGK equation discretized in microscopic velocity space then reads

$$\partial_t f_i + (\boldsymbol{\xi}_i \cdot \boldsymbol{\nabla}) f_i = -\frac{1}{\tau}\left(f_i - f_i^{(0)}(\rho, \boldsymbol{u})\right). \tag{33}$$

As pointed out above, the set populations (f_i and $f_i^{(0)}$) live in a q-dimensional space which means that they can be represented on a q-dimensional basis. In d'Humières [1992], d'Humières et al. [2002] or Dellar [2003] different bases are proposed for the expansion of the complete populations but never used to express the equilibrium distribution. Here we propose to expand the equilibrium population on a complete basis as well. To this aim we will use an interesting property of the D2Q9 and the D3Q27 lattices, which is that the complete 9- and 27-dimensional bases can be expressed in Hermite polynomials, a property that does not hold for the D3Q15 and D3Q19 quadratures. This property makes them particularly appealing in order to reuse all the calculations performed in the previous section. The distribution function is therefore written as (in 2D)

$$\begin{aligned} f_i =& w_i \left(\rho + \frac{\boldsymbol{\xi}_i \cdot (\rho \boldsymbol{u})}{c_s^2} + \frac{1}{2c_s^4}\mathcal{H}_i^{(2)} : \boldsymbol{a}^{(2)} \right. \\ &\left. + \frac{1}{2c_s^6}\left(\mathcal{H}_{ixxy}^{(3)} a_{xxy}^{(3)} + \mathcal{H}_{ixyy}^{(3)} a_{xyy}^{(3)}\right) + \frac{1}{4c_s^8}\mathcal{H}_{ixxyy}^{(4)} a_{xxyy}^{(4)}\right). \end{aligned} \tag{34}$$

Respectively the equilibrium and off-equilibrium parts are expanded as

$$\begin{aligned} f_i^{(0)} =& w_i \rho \left(1 + \frac{\boldsymbol{\xi}_i \cdot \boldsymbol{u}}{c_s^2} + \frac{1}{2c_s^4}\mathcal{H}_i^{(2)} : \boldsymbol{u}\boldsymbol{u} \right. \\ &\left. + \frac{1}{2c_s^6}\left(\mathcal{H}_{ixxy}^{(3)} u_x^2 u_y + \mathcal{H}_{ixyy}^{(3)} u_x u_y^2\right) + \frac{1}{4c_s^8}\mathcal{H}_{ixxyy}^{(4)} u_x^2 u_y^2\right) \end{aligned} \tag{35}$$

$$\begin{aligned} f_i^{(1)} =& w_i \left(\frac{1}{2c_s^4}\mathcal{H}_i^{(2)} : \boldsymbol{a}_1^{(2)} + \frac{1}{2c_s^6}\left(\mathcal{H}_{ixxy}^{(3)} a_{1,xxy}^{(3)} + \mathcal{H}_{ixyy}^{(3)} a_{1,xyy}^{(3)}\right) \right. \\ &\left. + \frac{1}{4c_s^8}\mathcal{H}_{ixxyy}^{(4)} a_{1,xxyy}^{(4)}\right). \end{aligned} \tag{36}$$

In 3D the equivalent expressions are given by

$$
\begin{aligned}
f_i =& w_i \Bigg(\rho + \frac{\boldsymbol{\xi}_i \cdot (\rho \boldsymbol{u})}{c_s^2} + \frac{1}{2c_s^4} \mathcal{H}_i^{(2)} : \boldsymbol{a}^{(2)} \\
&+ \frac{1}{2c_s^6} \Big(\mathcal{H}_{ixxy}^{(3)} a_{xxy}^{(3)} + \mathcal{H}_{ixxz}^{(3)} a_{xxz}^{(3)} + \mathcal{H}_{ixyy}^{(3)} a_{xyy}^{(3)} + \mathcal{H}_{ixzz}^{(3)} a_{xzz}^{(3)} \\
&\qquad + \mathcal{H}_{iyzz}^{(3)} a_{yzz}^{(3)} + \mathcal{H}_{iyyz}^{(3)} a_{yyz}^{(3)} + 2\mathcal{H}_{ixyz}^{(3)} a_{xyz}^{(3)} \Big) \\
&+ \frac{1}{4c_s^8} \Big(\mathcal{H}_{ixxyy}^{(4)} a_{xxyy}^{(4)} + \mathcal{H}_{ixxzz}^{(4)} a_{xxzz}^{(4)} + \mathcal{H}_{iyyzz}^{(4)} a_{yyzz}^{(4)} \\
&\qquad + 2 \left(\mathcal{H}_{ixyzz}^{(4)} a_{xyzz}^{(4)} + \mathcal{H}_{ixyyz}^{(4)} a_{xyyz}^{(4)} + \mathcal{H}_{ixxyz}^{(4)} a_{xxyz}^{(4)} \right) \Big) \\
&+ \frac{1}{4c_s^{10}} \Big(\mathcal{H}_{ixxyzz}^{(5)} a_{xxyzz}^{(5)} + \mathcal{H}_{ixxyyz}^{(5)} a_{xxyyz}^{(5)} + \mathcal{H}_{ixyyzz}^{(5)} a_{xyyzz}^{(5)} \Big) \\
&+ \frac{1}{8c_s^{12}} \mathcal{H}_{ixxyyzz}^{(6)} a_{xxyyzz}^{(6)} \Bigg),
\end{aligned} \tag{37}
$$

$$
\begin{aligned}
f_i^{(0)} =& w_i \rho \Bigg(1 + \frac{\boldsymbol{\xi}_i \cdot \boldsymbol{u}}{c_s^2} + \frac{1}{2c_s^4} \mathcal{H}_i^{(2)} : \boldsymbol{u}\boldsymbol{u} \\
&+ \frac{1}{2c_s^6} \Big(\mathcal{H}_{ixxy}^{(3)} u_x^2 u_y + \mathcal{H}_{ixxz}^{(3)} u_x^2 u_z + \mathcal{H}_{ixyy}^{(3)} u_x u_y^2 + \mathcal{H}_{ixzz}^{(3)} u_x u_z^2 \\
&\qquad + \mathcal{H}_{iyzz}^{(3)} u_y u_z^2 + \mathcal{H}_{iyyz}^{(3)} u_y^2 u_z + 2\mathcal{H}_{ixyz}^{(3)} u_x u_y u_z \Big) \\
&+ \frac{1}{4c_s^8} \Big(\mathcal{H}_{ixxyy}^{(4)} u_x^2 u_y^2 + \mathcal{H}_{ixxzz}^{(4)} u_x^2 u_z^2 + \mathcal{H}_{iyyzz}^{(4)} u_y^2 u_z^2 \\
&\qquad + 2 \left(\mathcal{H}_{ixyzz}^{(4)} u_x u_y u_z^2 + \mathcal{H}_{ixyyz}^{(4)} u_x u_y^2 u_z + \mathcal{H}_{ixxyz}^{(4)} u_x^2 u_y u_z \right) \Big) \\
&+ \frac{1}{4c_s^{10}} \Big(\mathcal{H}_{ixxyzz}^{(5)} u_x^2 u_y u_z^2 + \mathcal{H}_{ixxyyz}^{(5)} u_x^2 u_y^2 u_z + \mathcal{H}_{ixyyzz}^{(5)} u_x u_y^2 u_z^2 \Big) \\
&+ \frac{1}{8c_s^{12}} \mathcal{H}_{ixxyyzz}^{(6)} u_x^2 u_y^2 u_z^2 \Bigg),
\end{aligned} \tag{38}
$$

$$
\begin{aligned}
f_i^{(1)} =& w_i \Bigg(\frac{1}{2c_s^4} \mathcal{H}_i^{(2)} : \boldsymbol{a}_1^{(2)} \\
&+ \frac{1}{2c_s^6} \Big(\mathcal{H}_{ixxy}^{(3)} a_{1,xxy}^{(3)} + \mathcal{H}_{ixxz}^{(3)} a_{1,xxz}^{(3)} + \mathcal{H}_{ixyy}^{(3)} a_{1,xyy}^{(3)} + \mathcal{H}_{ixzz}^{(3)} a_{1,xzz}^{(3)} \\
&\qquad + \mathcal{H}_{iyzz}^{(3)} a_{1,yzz}^{(3)} + \mathcal{H}_{iyyz}^{(3)} a_{1,yyz}^{(3)} + 2\mathcal{H}_{ixyz}^{(3)} a_{1,xyz}^{(3)} \Big) \\
&+ \frac{1}{4c_s^8} \Big(\mathcal{H}_{ixxyy}^{(4)} a_{1,xxyy}^{(4)} + \mathcal{H}_{ixxzz}^{(4)} a_{1,xxzz}^{(4)} + \mathcal{H}_{iyyzz}^{(4)} a_{1,yyzz}^{(4)} \\
&\qquad + 2 \left(\mathcal{H}_{ixyzz}^{(4)} a_{1,xyzz}^{(4)} + \mathcal{H}_{ixyyz}^{(4)} a_{1,xyyz}^{(4)} + \mathcal{H}_{ixxyz}^{(4)} a_{1,xxyz}^{(4)} \right) \Big) \\
&+ \frac{1}{4c_s^{10}} \Big(\mathcal{H}_{ixxyzz}^{(5)} a_{1,xxyzz}^{(5)} + \mathcal{H}_{ixxyyz}^{(5)} a_{1,xxyyz}^{(5)} + \mathcal{H}_{ixyyzz}^{(5)} a_{1,xyyzz}^{(5)} \Big) \\
&+ \frac{1}{8c_s^{12}} \mathcal{H}_{ixxyyzz}^{(6)} a_{1,xxyyzz}^{(6)} \Bigg).
\end{aligned} \tag{39}
$$

The Hermite coefficients of the equilibrium distribution are the ones obtained from of the continuous equilibrium distribution for both the 2D and 3D cases, simplifying the computations. Another important remark is that not all the Hermite polynomials are used at each order. This is due to the fact that the quadrature is not accurate enough to represent exactly all the Hermite polynomials, but only the ones that are used in the formulas above.

3.3 Chapman–Enskog expansion of the model

The Chapman–Enskog expansion of this model asymptotically leads to the following constitutive equation for $\boldsymbol{a}_1^{(2)}$ in three dimensions

$$a_{1,xx}^{(2)} = -2c_s^2\rho\tau S_{xx} + \underbrace{\tau\partial_x(\rho u_x^3)}_{*}, \tag{40}$$

$$a_{1,xy}^{(2)} = -2c_s^2\rho\tau S_{xy}, \tag{41}$$

$$a_{1,xz}^{(2)} = -2c_s^2\rho\tau S_{xz}, \tag{42}$$

$$a_{1,yy}^{(2)} = -2c_s^2\rho\tau S_{yy} + \underbrace{\tau\partial_y(\rho u_y^3)}_{*}, \tag{43}$$

$$a_{1,yz}^{(2)} = -2c_s^2\rho\tau S_{yz}, \tag{44}$$

$$a_{1,zz}^{(2)} = -2c_s^2\rho\tau S_{zz} + \underbrace{\tau\partial_z(\rho u_z^3)}_{*}, \tag{45}$$

where the "$*$" terms are $\emptyset(\mathrm{Ma}^3)$ order error terms which are not present in the continuous case (see Eq. (25)). In the case of the order two standard BGK model (where $f_i^{(0)}$ is only expanded up to order two in Hermite polynomials) it reads

$$a_{1,xx}^{(2)} = -2c_s^2\rho\tau S_{xx} + \tau(\partial_x(\rho u_x^3)\underbrace{+\partial_y(\rho u_y u_x^2) + \partial_z(\rho u_z u_x^2)}_{**}), \tag{46}$$

$$a_{1,xy}^{(2)} = -2c_s^2\rho\tau S_{xy}\underbrace{+\tau(\partial_x(\rho u_x^2 u_y) + \partial_y(\rho u_x u_y^2) + \partial_z(\rho u_x u_y u_z))}_{**}, \tag{47}$$

$$a_{1,xz}^{(2)} = -2c_s^2\rho\tau S_{xz}\underbrace{+\tau(\partial_y(\rho u_x u_y u_z) + \partial_x(\rho u_z u_x^2) + \partial_z(\rho u_x u_z^2))}_{**}, \tag{48}$$

$$a_{1,yy}^{(2)} = -2c_s^2\rho\tau S_{yy} + \tau(\partial_y(\rho u_y^3)\underbrace{+\partial_x(\rho u_x u_y^2) + \partial_z(\rho u_z u_y^2)}_{**}), \tag{49}$$

$$a_{1,yz}^{(2)} = -2c_s^2\rho\tau S_{yz}\underbrace{+\tau(\partial_x(\rho u_x u_y u_z) + \partial_y(\rho u_z u_y^2) + \partial_z(\rho u_y u_z^2))}_{**}, \tag{50}$$

$$a_{1,zz}^{(2)} = -2c_s^2\rho\tau S_{zz} + \tau(\partial_z(\rho u_z^3)\underbrace{+\partial_x(\rho u_x u_z^2) + \partial_y(\rho u_y u_z^2)}_{**}), \tag{51}$$

where the "$**$" terms are the terms that are not present anymore in the new model. One can see that in our case the non-diagonal terms are exact.

Furthermore since we now expand the distribution function up to a limited order in Hermite polynomials the relations of Eq. (31) are not anymore

exactly verified. Nevertheless the difference between the exact relation and the error committed is compatible with the low compressibility approximation of the scheme (low Mach number approximation). In other terms Eq. (31) reads in the discrete case

$$a^{(n)}_{1,\alpha_1\ldots\alpha_n} = a^{(n-1)}_{1,\alpha_1\ldots\alpha_{n-1}} u_{\alpha_n} + \left(u_{\alpha_1}\ldots u_{\alpha_{n-2}} a^{(2)}_{1,\alpha_{n-1}\alpha_n} + \mathrm{perm}(\alpha_n) \right) + \emptyset(\mathrm{Ma}^{n+1}), \tag{52}$$

where $\emptyset$ stands for the order of the error committed. These terms are spurious terms that are due to quadrature (discretization in velocity space) errors in the expansion and are assumed to be small because they are one order higher in physical velocity. For a more detailed expression for the $\emptyset(\mathrm{Ma}^{n+1})$ terms see B.

3.4 Time-space discretization

The time space discretization of Eq. (33) is done as usual by integrating it along characteristics with the trapezoidal rule and making the following change of variables (see Dellar [2001] for example)

$$\bar{f}_i = \bar{f}_i + \frac{1}{2\tau}\left(\bar{f}_i - f_i^{(0)}\right). \tag{53}$$

This leads to the following lattice Boltzmann method scheme

$$\bar{f}_i(\boldsymbol{x} + \boldsymbol{\xi}_i, t+1) = \bar{f}_i(\boldsymbol{x}, t) - \frac{1}{\bar{\tau}}\left(\bar{f}_i(\boldsymbol{x}, t) - f_i^{(0)}(\boldsymbol{x}, t)\right), \tag{54}$$

where $\bar{\tau} \equiv \tau + 1/2$. From now on the "bar" is omitted for brevity in the notations.

3.5 Regularization scheme

The numerical scheme used here is given by Eq. (54) where f_i is "regularized" at each iteration as done in Latt and Chopard [2006]

$$f_i = f_i^{(0)} + f_i^{(1)}, \tag{55}$$

where $f_i^{(1)}$ is computed with Eqs. (36) or (39) depending on the dimension of the physical space. Furthermore the Hermite coefficients of Eqs. (36) and (39) ($\boldsymbol{a}_1^{(n)}$, with $n > 2$) are evaluated thanks to the recursive formulation of Eq. (31). For efficiency reasons Eq. (54) can thus be rewritten as

$$f_i(\boldsymbol{x} + \boldsymbol{\xi}_i, t+1) = f_i^{(0)} + \left(1 - \frac{1}{\tau}\right) f_i^{(1)}. \tag{56}$$

This is the novel scheme proposed in this paper. The model will be validated in Sec. 4 and a comparison with an existing multiple-relaxation-time model will be performed.

3.6 Von Neumann linear stability analysis

The aim of this section is to perform the linear stability analysis of the scheme. More details about the Von Neumann stability analysis of the lattice Boltzmann method can be found among others in Lallemand and Luo [2000], Ricot et al. [2009], Xu and Sagaut [2011], Xu et al. [2012].

By decomposing the distribution function into the sum of a stationary part (noted $\bar{f}_i$ which must not be confused with the $\bar{f}$ of Subsec. 3.4) and a small fluctuating part, noted f'_i,

$$f_i = \bar{f}_i + f'_i, \tag{57}$$

and by defining Ω_i as the r.h.s. of Eq. (56)

$$\Omega_i \equiv f_i^{(0)} + \left(1 - \frac{1}{\tau}\right) f_i^{(1)}, \tag{58}$$

the linearized lattice Boltzmann scheme is found to be given by

$$f'_i(\boldsymbol{x} + \boldsymbol{\xi}_i, t+1) = \sum_j \Lambda_{ij} f'_j(\boldsymbol{x}, t), \tag{59}$$

where $\boldsymbol{\Lambda}$ is defined as

$$\Lambda_{ij} = \left.\frac{\partial \Omega_i}{\partial f_j}\right|_{f_j = \bar{f}_j}. \tag{60}$$

Working in Fourier space and looking for plane wave solutions Eq. (59) becomes

$$f'_l(\boldsymbol{k}, t+1) = \sum_{j,k} A^{-1}_{lj} \Lambda_{jk} f'_k(\boldsymbol{k}, t), \tag{61}$$

where $A^{-1}_{jk} = \delta_{jk} \exp\left(-i\boldsymbol{k} \cdot \boldsymbol{\xi}_j\right)$, with δ_{jk} the Kronecker symbol and $i = \sqrt{-1}$.

The eigenvalues, λ_j, of the matrix $\boldsymbol{A}^{-1}\boldsymbol{\Lambda}$ allow to obtain the dispersion-dissipation relations of the numerical scheme, $\omega_j(\boldsymbol{k}) = i \log \lambda_j$. While an analytic approach is used to determine these eigenvalues in Lallemand and Luo [2000], here we simply used a linear algebra package to determine numerically these eigenvalues.

The Von Neumann stability analysis of the Navier–Stokes gives the following dispersion-dissipation relations

$$\mathrm{Re}(\omega_\pm) = \pm ||\boldsymbol{k}|| c_s + \boldsymbol{k} \cdot \boldsymbol{u}, \tag{62}$$

$$\mathrm{Im}(\omega_\pm) = -||\boldsymbol{k}||^2 \frac{1}{2} \left(\frac{2D-2}{D}\nu + \eta\right), \tag{63}$$

$$\mathrm{Re}(\omega_s) = \boldsymbol{k} \cdot \boldsymbol{u}, \tag{64}$$

$$\mathrm{Im}(\omega_s) = -||\boldsymbol{k}||^2 \nu, \tag{65}$$

where $\eta = \frac{2}{D}\nu$ for the BGK model.

We now compare the eigenvalues of the collision operator of the present model we the ones obtained for the MRT model proposed by Lallemand and Luo [2000]. The stability analysis depicted in this section has been performed for $\tau = 0.5001$ and $\boldsymbol{u} = (0.2, 0)$ (corresponding to Ma $= 0.346$). As one can see from Fig. 1 the dispersion relations for the present scheme are relatively similar to the ones obtained with an MRT approach except for the shear mode

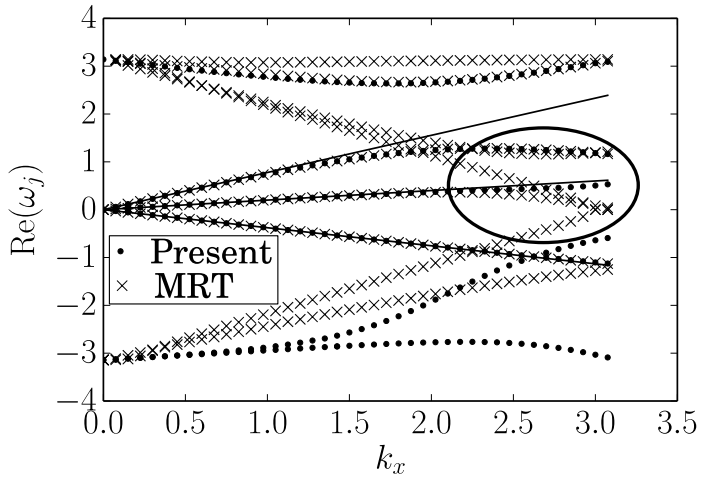

Figure 1: Dispersion with respect to k_x ($k_y = 0$) for the present model and the MRT model with the $u_x = 0.2$, for the D2Q9 lattice, and $\tau = 0.5001$. This circled region highlights the region where there is a significant improvement of the dispersion relation of the present model as compared to the MRT model.

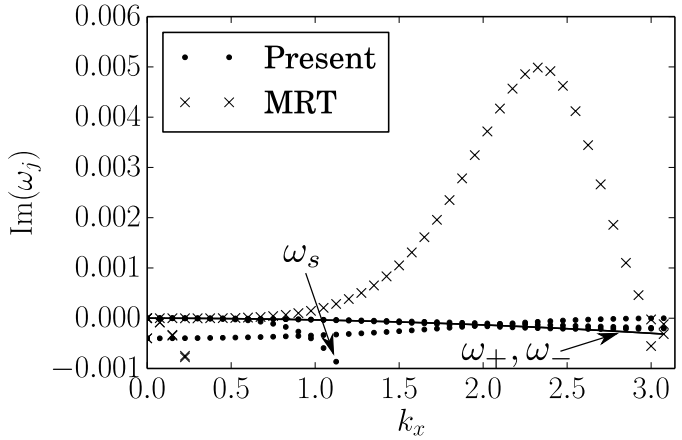

Figure 2: Dissipation (right) with respect to k_x ($k_y = 0$) for the present model and the MRT model with the $u_x = 0.2$, for the D2Q9 lattice, and $\tau = 0.5001$.

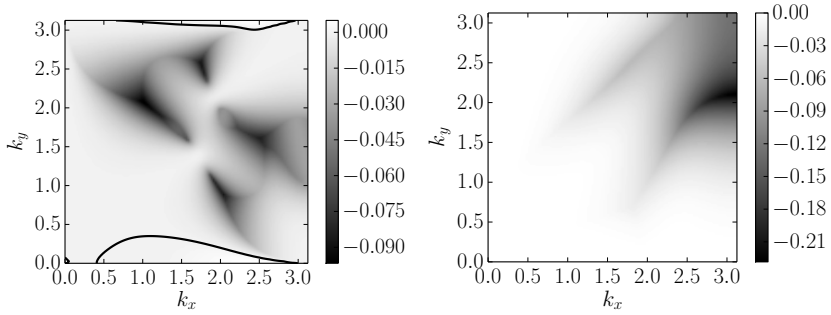

Figure 3: Maximal value of the dissipation, $\max_j \omega_j(\boldsymbol{k})$, for the MRT (left) and present (right) models with $u_x = 0.2$, for the D2Q9 lattice, and $\tau = 0.5001$. The solid line represents the isocontour where $\max_j \omega_j(\boldsymbol{k}) = 0$.

where the dispersion relation remains very close to the Navier–Stokes result until $k_x = \pi$ which is not the case for the MRT (see the circled region of Fig. 1). For the dissipation (see Fig. 2) one clearly sees that for $k_y = 0$ there is no unstable mode for the present model ($\mathrm{Im}(\omega_j) < 0, \forall k_x, j$) while this is not the case for the MRT model. Furthermore one can also notice that while the acoustic modes are only weakly dissipated, except for ω_s, (and therefore the proposed scheme could be very suitable for aeroacoustic simulations) the other spurious modes are dissipated very fast and therefore the scheme should suffer of less numerical instabilities. The increased linear stability of the model is depicted in Fig. 3 where one can see that the imaginary part of the eigenvalues of the numerical scheme is always negative and therefore the scheme has an unconditional linear stability. This feature is not present in the case of the MRT model as for some values of $\boldsymbol{k}$ the imaginary part of the eigenvalues of the evolution operator become positive. Of course as one increases the magnitude of the velocity unstable modes will start to appear. The unstable modes start to appear at $u_x = 0.248$ (corresponding to $\mathrm{Ma} = 0.43$) for $\tau = 0.5001$ as shown on Fig. 4.

3.7 Boundary conditions

The aim of this subsection is not to give a detailed view of the way to implement boundary conditions since this topic is extensively treated in the literature (see Latt et al. [2008], Malaspinas et al. [2011], Zou and He [1997], Inamuro et al. [1995], Skordos [1993] among others for some references). It rather explains how the proposed regularization model is compatible with all the cited boundary conditions.

One way to deal with Dirichlet boundary conditions in the lattice Boltzmann method is to use the regularized procedure described in Latt et al. [2008] for example. The generic idea is to impose a velocity $\boldsymbol{u}_{\mathrm{bc}}$ at the boundary. First one uses the symmetries of the lattice to compute ρ. Then it is possible to compute $f_i^{(0)}$ (which only depends on ρ and $\boldsymbol{u}_{\mathrm{bc}}$). Finally $\boldsymbol{P}^{(1)}$ can be computed using a finite difference scheme through $\boldsymbol{S}$ or by using the symmetries of the lattice

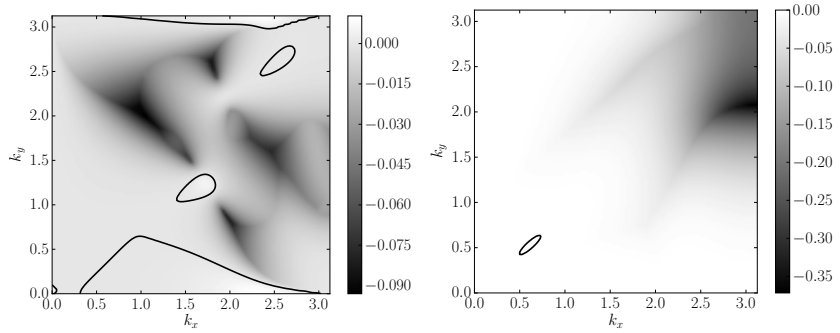

Figure 4: Maximal value of the dissipation, $\max_j \omega_j(\boldsymbol{k})$, for the MRT (left) and present (right) models with $u_x = 0.248$, for the D2Q9 lattice, and $\tau = 0.5001$. The solid line represents the isocontour where $\max_j \omega_j(\boldsymbol{k}) = 0$.

(see Latt et al. [2008]). Then $f_i^{(1)}$ is computed by using the following formula

$$f_i^{(1)} = \frac{w_i}{2c_s^4} \mathcal{H}_i^{(2)} : \boldsymbol{P}^{(1)}.$$

We notice that this formula is actually exact if $\boldsymbol{u}_{\rm bc} = 0$. By replacing $\boldsymbol{u}_{\rm bc}$ by zero in Eq. (36) or (39) one is simply left with the equation above. Then if $\boldsymbol{u}_{\rm bc} \neq 0$, the procedure is exactly the same as for the two strategies discussed above and we should simply use Eqs. (36) or (39) for the computation of $f_i^{(1)}$. Finally one simply replaces all the populations on the boundary mesh point with the regularization formula (55).

3.8 Differences with existing stabilization techniques

Apart from the MRT-LBM there exists different techniques to increase the stability and accuracy of the BGK-LBM scheme. In this subsection we discuss the major distinctions between the present scheme and some of these approaches. We will limit the discussion to the regularization, entropic, and selective viscosity filter techniques.

3.8.1 The regularized model

The existing class of regularized models (see Zhang et al. [2006], Latt and Chopard [2006]) belongs to the same family as the model presented here. The general idea is the same as the one used for the present model. The collision operator is the same as Eq. (56)

$$f_i(\boldsymbol{x} + \boldsymbol{\xi}_i, t+1) = f_i^{(0)} + \left(1 - \frac{1}{\tau}\right) f_i^{(1)},$$

but instead of using the equilibrium distribution of Eqs. (35) (in 2D) or (38) (in 3D), and off-equilibrium distribution of Eqs. (36) (in 2D) or (39) (in 3D), one

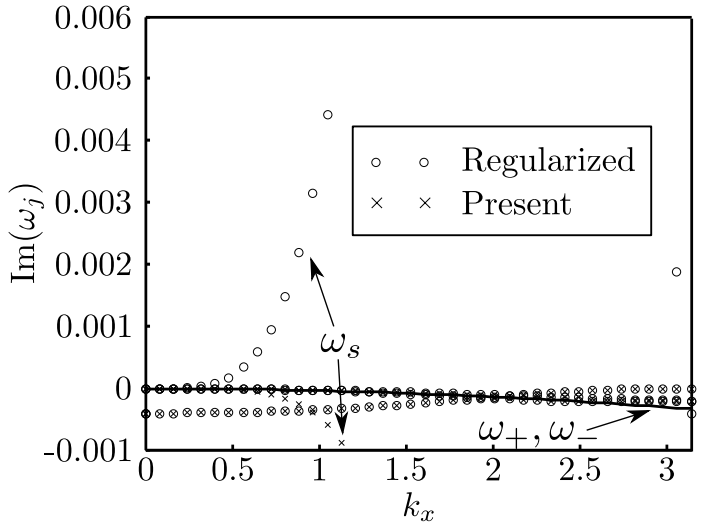

Figure 5: Dissipation (right) with respect to k_x ($k_y = 0$) for the present model and the MRT model with the $u_x = 0.2$, for the D2Q9 lattice, and $\tau = 0.5001$.

truncates the series at order two in Hermite polynomials, which amounts to use

$$f_i^{(0)} = w_i \rho \left(1 + \frac{\boldsymbol{\xi}_i \cdot \boldsymbol{u}}{c_s^2} + \frac{1}{2c_s^4} \mathcal{H}_i^{(2)} : \boldsymbol{u}\boldsymbol{u} \right), \tag{66}$$

$$f_i^{(1)} = \frac{w_i}{2c_s^4} \mathcal{H}_i^{(2)} : \boldsymbol{a}_1^{(2)}. \tag{67}$$

This regularization technique removes all the moments of order higher than two in Hermite polynomials from the distribution function. These are considered as negligible in the asymptotic limit of the weakly compressible Navier–Stokes equation. The removal of these higher order terms affect the accuracy of the constitutive equation for the stress tensor $\boldsymbol{a}_1^{(2)} = \boldsymbol{P}^{(1)}$ as shown in Eqs. (40)-(45) and Eqs. (46)-(51). The present regularization not only provides a more accurate constitutive equation for the deviatoric stress but also preserves the recursive relation of the $\boldsymbol{a}_1^{(n)}$ (for $n \geq 3$) terms. These differences lead to a major difference for the linear stability analysis of the two schemes. A comparison for of the dissipation (see Subsec. 3.6) for $u_x = 0.2$ and $\tau = 0.5001$ is shown in Fig. 5. One can see that while the $\omega_\pm$ eigenvalues have very similar values for both models, the difference lies in the ω_s eigenvalue. For the regularized model this eigenvalue is positive (and therefore an unstable mode exists) while it is negative for the present model. Therefore one expects the present model to exhibit a much more stable behavior.

3.8.2 The entropic model

The entropic model (see among other Ansumali and Karlin [2002], Boghosian et al. [2003], Chikatamarla et al. [2006]) is based on a different philosophy for the construction of the numerical scheme. The major difference is the existence

of an H-function defined as

$$H = \sum_i f_i \log \frac{f_i}{w_i}. \tag{68}$$

The assumption is then made that there exists a discrete H-theorem which states that

1. The equilibrium distribution, $f_i^{(0)}$ minimizes the H function under the constrains that $\sum_i f_i^{(0)} = \rho$ and $\sum_i \boldsymbol{\xi}_i f_i^{(0)} = \rho \boldsymbol{u}$.
2. The H function is monotonically decreasing.

This second condition is imposed through the following collision operator

$$f(\boldsymbol{x} + \boldsymbol{\xi}_i, t+1) = f_i - \frac{\alpha}{2\tau}\left(f_i - f_i^{(0)}\right), \tag{69}$$

where $\alpha > 0$ is computed such that

$$H(f_i - \alpha(f_i - f_i^{(0)})) = H(f_i). \tag{70}$$

The collision operator of the entropic model guarantees an unconditional stability of the scheme. This comes nevertheless at a high computational cost since at each point and at each time the above non-linear implicit equation must be solved. As shown in several references (see Malaspinas et al. [2008] among others) the presence of the α parameter has as an effect to locally increase the viscosity (and therefore the dissipation). Therefore one would expect that the dissipation of the entropic scheme would be more important and therefore less suitable for acoustic propagation for example.

3.8.3 The selective viscosity model

In the selective viscosity model proposed by Ricot et al. [2009] the basic idea is to use the standard BGK-LBM collision operator (see Eq. (54)) and to increase the stability of the model by applying a low-pass filter on the f_i at each point and at each time step. The filtering operation is defined as

$$\langle f_i(\boldsymbol{x}, t)\rangle = f_i(\boldsymbol{x}, t) - \sigma \sum_{j=1}^{D} \sum_{n=-N}^{N} d_n f_i(\boldsymbol{x} + n\boldsymbol{e}_j), \tag{71}$$

where $\boldsymbol{e}_j$ are the D unit basis vectors of the Cartesian coordinate system, the d_n are the $2N+1$ filter coefficients, and $\sigma \in [0,1]$ is the strength of the filter. This filtering operation removes the high frequency oscillations responsible for the numerical instabilities appearing in the model. The different filters proposed in Ricot et al. [2009] involve non-local computations (the filters have width between three and nine mesh points) that impacts greatly the computational efficiency of the scheme since not only more operations must be performed at each mesh point but also the amount of communications (which are crucial for parallel efficiency) is also increased. In the model presented here no such non-local operations are performed reducing the computational cost with respect to the selective viscosity models.

Furthermore the filtering operation implies the existence of a cutoff which removes the high wavenumber components of the flow. As shown in Ricot et al. [2009] the large wavenumber dissipation is greatly enhanced in order to stabilize the numerical scheme. All the $\mathrm{Im}(\omega_j)$ in the Von Neumann stability analysis are greatly decreased after the cutoff value which decreases the accuracy of the propagation of high wavenumber components of the flow. In the present model only the dissipation of ω_s is increased and $\omega_\pm$ are left untouched with respect to the LBM-BGK scheme which should provide a better accuracy for acoustic applications.

4 Benchmarks

In order to validate the model we are going to study a 2D and a 3D case, namely the dipole-wall interaction, and the turbulent jet. Both these flows are challenging from the numerical point of view since they exhibit a turbulent behavior (2D as well as 3D turbulence).

4.1 Dipole–wall interaction

This benchmark is based on the works of Clercx and Bruneau [2006] and Latt and Chopard [2007]. It analyzes the time evolution of a self-propelled dipole confined within a 2D box. The geometry of the box is a square domain $[-L, L] \times [-L, L]$, surrounded by no-slip walls. The initial condition describes two counter-rotating monopoles, one with positive core vorticity at the position (x_1, y_1) and the other one with negative core vorticity at (x_2, y_2). This is obtained with an initial velocity field $\boldsymbol{u}_0 = (u_x, u_y)$ which reads as follows in dimensionless variables

$$u_x = -\frac{1}{2} \|\omega_e\| (y - y_1) \mathrm{e}^{-(r_1/r_0)^2} + \frac{1}{2} \|\omega_e\| (y - y_2) \mathrm{e}^{-(r_2/r_0)^2}, \tag{72}$$

$$u_y = +\frac{1}{2} \|\omega_e\| (x - x_1) \mathrm{e}^{-(r_1/r_0)^2} - \frac{1}{2} \|\omega_e\| (x - x_2) \mathrm{e}^{-(r_2/r_0)^2}. \tag{73}$$

Here, $r_i = \sqrt{(x - x_i)^2 + (y - y_i)^2}$, defines the distance to the monopole centers. The parameter r_0 labels the diameter of a monopole and ω_e its core vorticity.

The quantity we are interested in monitoring is the average enstrophy which is defined by

$$\langle \Omega \rangle (t) = \frac{1}{2} \int_{-1}^{1} \int_{-1}^{1} \omega^2(\boldsymbol{x}, t) \mathrm{d}x \mathrm{d}y, \tag{74}$$

where $\omega = \partial_x u_y - \partial_y u_x$ is the flow vorticity.

Under the actions of viscous forces, the dipole described by Eqs. (72) and (73) develops a net momentum in the positive x-direction and is self-propelled towards the right wall. The collision between the dipole and the wall is characterized by a 2D turbulent dynamics where the wall acts as a source of small-scale vortices that originate from detached boundary layers. After the first collision the monopoles under the action of viscosity are re-propelled against the wall. These collisions give rise to two peaks of enstrophy (see Fig. 6). The value of these local maxima will be used for comparison with the results obtained with a spectral method in Clercx and Bruneau [2006]. Several snapshot of the dynamics of the dipole–wall collision can be found on Fig. 7.

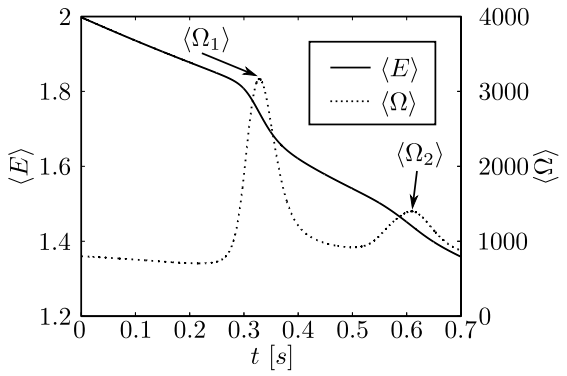

Figure 6: Average energy (plain line) and average enstrophy (dotted line) evolution with time. The two enstrophy peaks $\langle \Omega_1 \rangle$ and $\langle \Omega_2 \rangle$ are highlighted.

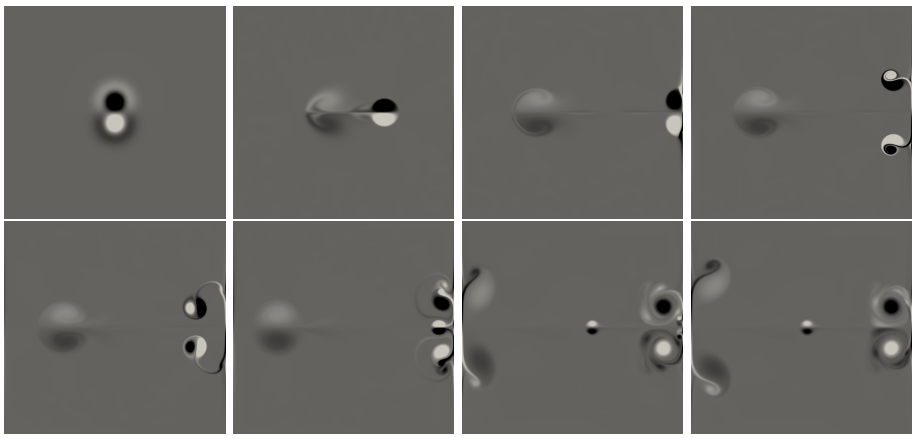

Figure 7: Snapshot of the vorticity at $t = 0, 0.15, 0.0.32, 0.4, 0.48, 0.64, 0.72.0.8$ from left to right and top to bottom. Black is for positive and white for negative vorticity.

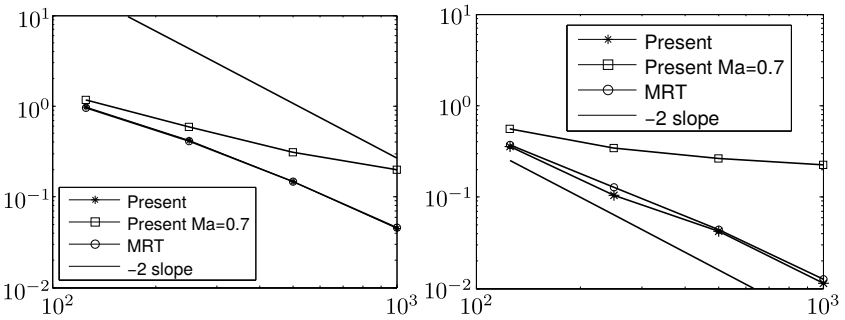

Figure 8: Numerical accuracy in the 2D dipole-wall collision flow for the two enstrophy peaks, (left) $\omega_1 = 3313$, and (right) $\omega_2 = 1418$. The error curves for the enstrophy peak obtained with the present scheme and the MRT scheme.

In this benchmark the initial core vorticity of the monopoles is fixed to $\omega_e = 299.5286$. Furthermore, the Reynolds number and the monopole radius are set to $\mathrm{Re} = LU/\nu = 2500$ and $r_0 = 0.1$. The positions of the monopole centers are $(x_1, y_1) = (0, 0.1)$ and $(x_2, y_2) = (0, -0.1)$. The approach of Latt and Chopard [2007] is used to set up the initial condition.

The error on the value of the enstrophy peak is the principal quantity of interest here. It is defined as

$$E_i = \left| \langle \Omega_i \rangle - \langle \Omega_{i,\mathrm{lb}} \rangle \right| / \langle \Omega_i \rangle, \tag{75}$$

where $i = 1, 2$ is the label of the enstrophy peak. The value of the enstrophy computed with the LBM (either the present model or the MRT model) is noted $\langle \Omega_{i,\mathrm{lb}} \rangle$. The reference value $\langle \Omega_i \rangle$ is the value found in Clercx and Bruneau [2006] and is given by $\langle \Omega_1 \rangle = 3313$ and $\langle \Omega_2 \rangle = 1418$. The convergence study is performed by keeping ν constant and modifying U_{lb} while varying the resolution N ($\mathrm{Re} = U_{\mathrm{lb}} N/\nu$). Here $U_{\mathrm{lb}} = 0.01N/125$ with $N = 125, 250, 500, 1000$. This rescaling of the velocity has as an effect to reduce the compressibility errors from the simulation (see Latt [2007]). As shown by Figs. 8 the difference in accuracy between methods is not dramatically different. The differences appear when one pushes the numerical scheme to more challenging Reynolds and Mach numbers.

In order to test the numerical stability and the ability to go to "higher" Mach numbers (but still lower than one) we also simulated the dipole at a maximal Ma number of 0.7 (corresponding to a characteristic velocity of $U_{\mathrm{lb}} = 0.032$) and $\mathrm{Re} = 2500$. At such high Mach number the MRT model was numerically unstable. The maximal stable reachable Mach number was of 0.46 (corresponding to characteristic velocity of $U_{\mathrm{lb}} = 0.02$). For this test the Mach number is kept constant and therefore one modifies the viscosity (in order to keep Re constant). By increasing the the resolution we do not remove the compressibility error terms (as discussed in Latt [2007]). This explains the first order decrease of the error observed in Fig. 8 and the lower accuracy of the results.

We notice that in this case the accuracy is much lower since the compressibility effects are much higher. Nevertheless the stability of the present model is highly enhanced with respect to the MRT model. Since such a "high" Mach

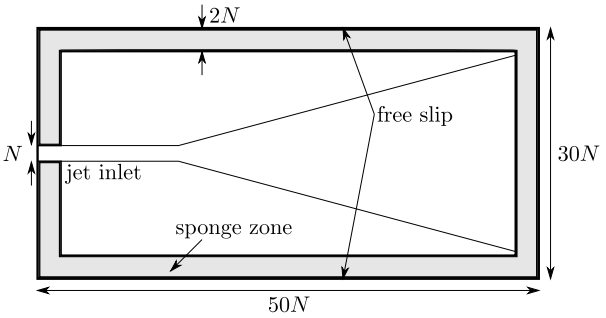

Figure 9: The turbulent jet computational domain.

number was not achievable with the MRT model.

4.2 Turbulent jet

In this section we will perform the simulation of a turbulent round jet (see Pope [2005]) at $\mathrm{Re} = NU/\nu = 6000$ with N and U being the diameter and the speed of the jet respectively. The aim will be to recover correctly the self similar behavior and the correct energy spectrum, and also correct pressure spectrum. The computational domain is depicted on Fig. 9. The domain size in units of the diameter of the jet was chosen to be of $[50, 30, 30] \times N$. In order to avoid as much as possible acoustic reflexions the sponge zones proposed by Xu and Sagaut [2013] were added in the domain. Furthermore a vortex ring (see Bogey et al. [2003] for example) is added at one diameter from the inlet to help the onset of the instability and allow for the development of turbulence in the flow. The Mach number of the flow is set to 0.4. The value is chosen to be rather large in order to really challenge the numerical accuracy and stability of the models.

The quantities of interest are defined as follows. The velocity, $\boldsymbol{u}(x, r, \theta, t)$, is given in cylindrical coordinates centered around the center of the jet. The mean axial velocity field at the center of the flow is given by

$$u_c(x) \equiv \langle u_x(x, 0, 0, t) \rangle \,, \tag{76}$$

where $\langle \cdot \rangle$ is the time average. The jet's half width, $r_{1/2}(x)$ is defined such that

$$\left\langle u_x(x, r_{1/2}(x), 0, t) \right\rangle = \frac{1}{2} u_c(x). \tag{77}$$

We will also study the Reynolds stresses $\left\langle u'_\alpha u'_\beta \right\rangle$, where

$$\boldsymbol{u}' = \boldsymbol{u} - \langle \boldsymbol{u} \rangle. \tag{78}$$

The simulation is performed with a very low resolution of $N = 10$ points in the diameter of the jet and with no explicit turbulence model for the case of the present model. For the MRT case a Smagorinsky model was needed (see Krafczyk et al. [2003], Malaspinas and Sagaut [2012]) in order to obtain stable results. The fact that no explicit turbulence model is needed for our novel

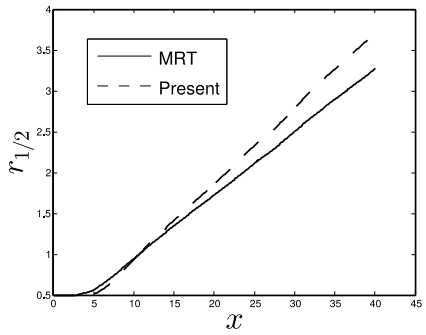

Figure 10: The jet's half width with respect to the position for the MRT and the present model. The spread rate is of respectively of $Sr_{\mathrm{MRT}} = 0.074$ and $Sr_{\mathrm{Present}} = 0.093$ for the MRT and present model.

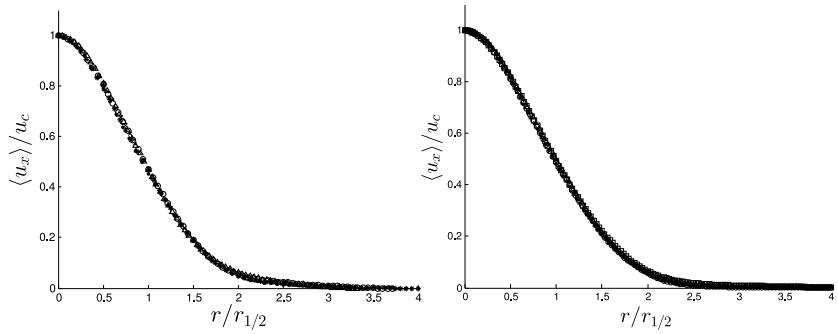

Figure 11: Non-dimensional velocity profile with respect to the rescaled position for the MRT (left) and the present (right) models. Five different x positions in part of the flow where the fluid is in a turbulent regime are depicted.

scheme seems to imply that the regularization operation has the effect of an implicit turbulence model and would deserve a more in-depth analysis.

Fig. 10 depicts $r_{1/2}(x)$ from which one can compute the spread rate $Sr = \mathrm{d}r_{1/2}/\mathrm{d}x$ of the jet for the MRT and the present model. Although both models exhibit a self-similar behavior since there is a linear growth of $r_{1/2}$, the value of the spread rates are significantly different. One has respectively $Sr_{\mathrm{MRT}} = 0.078$ and $Sr_{\mathrm{Present}} = 0.093$. The expected value of the spread rate is of roughly 0.1 (see Pope [2005]). Therefore the present model seems to provide a more accurate result than the MRT model.

As shown in Fig. 11 the self-similar behavior is observed for both models as for five different positions in the direction of the jet, the normalized average velocity profiles overlap for the MRT and for the present model. For the Reynolds stresses ($\langle {u'_x}^2 \rangle$, $\langle {u'_y}^2 \rangle$, and $\langle {u'_z}^2 \rangle$ respectively) which are depicted on Figs. 12-14 one can notice that the self similar behavior is shown for the present model. For the MRT model while close to the jet center the results seem self-similar (and also are coherent with what is observed with the present model), one can see that when going to $r/r_{1/2} \gtrsim 1.5$ the Reynolds stresses are not overlapping

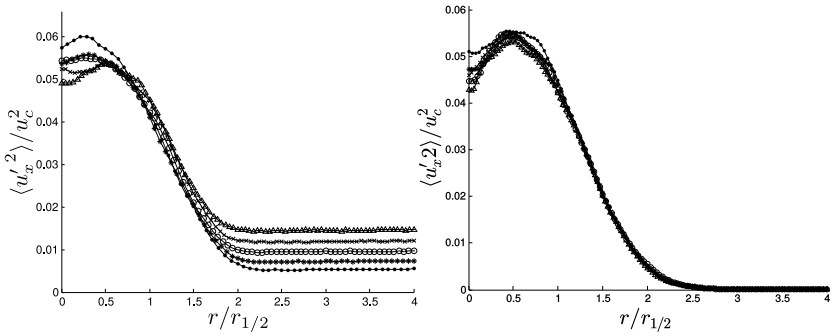

Figure 12: Non-dimensional Reynolds stress component $\langle u_x'^2 \rangle / u_c^2$ with respect to the rescaled position for the MRT (left) and the present (right) models. Five different x positions in part of the flow where the fluid is in a turbulent regime are depicted.

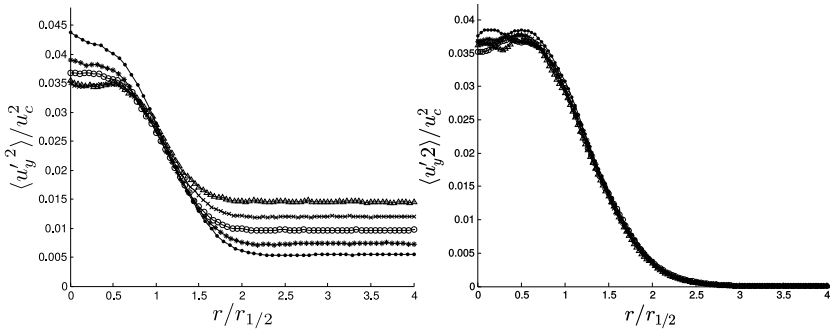

Figure 13: Non-dimensional Reynolds stress component $\langle u_y'^2 \rangle / u_c^2$ with respect to the rescaled position for the MRT (left) and the present (right) models. Five different x positions in part of the flow where the fluid is in a turbulent regime are depicted.

anymore and even worse, they are not converging towards zero as they should. This behavior can be explained by looking at the instantaneous velocity field at a given time. As one can see from Figs. 15, and 16 (which represent respectively instantaneous snapshots of the velocity norm and of the pressure fields) the results obtained with the present model are far less noisy and no spurious modes can be observed. The only "spurious" modes present in the present regularized model are due to the vortex ring used to trigger faster the transition to turbulence as seen on Fig. 16. For the MRT spurious modes can be observed in the pressure field although this model is expected (see Lallemand and Luo [2000], Xu and Sagaut [2011] for example) to dissipate the pressure waves at a higher rate than for BGK models.

Finally we also computed the energy and pressure power spectrum. One can see that for both the MRT and present model the $-5/3$ slope in the inertial range is recovered for the energy spectrum (see Fig. 17). For the pressure spectrum one expects to find a $-7/3$ slope in the inertial range as shown in George et al.

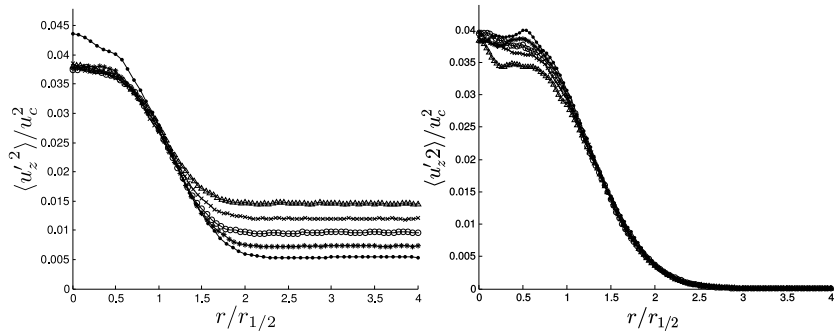

Figure 14: Non-dimensional Reynolds stress component $\langle u_z'^2 \rangle / u_c^2$ with respect to the rescaled position for the MRT (left) and the present (right) models. Five different x positions in part of the flow where the fluid is in a turbulent regime are depicted.

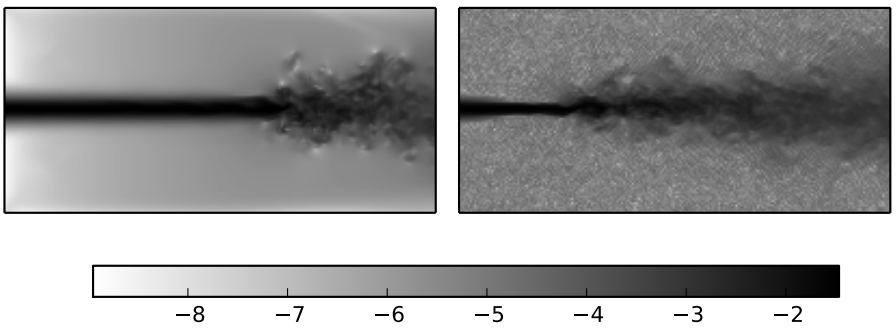

Figure 15: Instantaneous velocity norm for the turbulent jet for the present model (left) and the MRT model (right) in logscale. The sponge zone region is removed from these pictures.

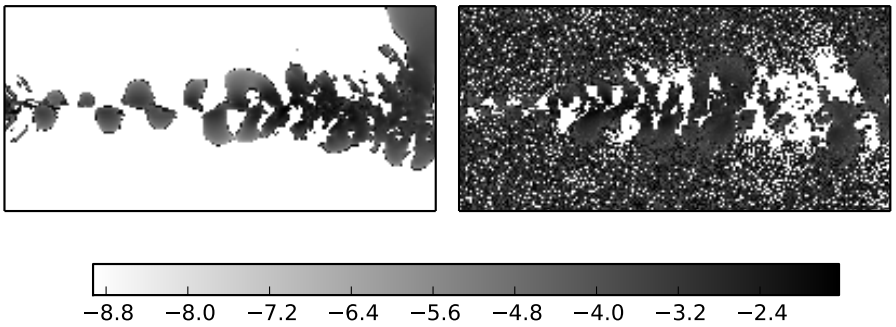

Figure 16: Pressure fluctuations for the turbulent jet for the present model (left) and the MRT model (right) in logscale. The colorbar scale has been reduced to allow seeing the small acoustic perturbations. The sponge zone region is removed from these pictures.

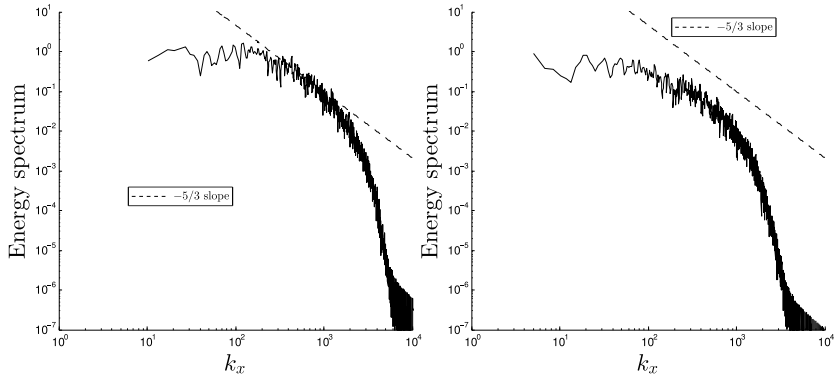

Figure 17: Energy power spectrum with respect to k_x for the MRT model (left) and the present model (right).

[1984]. While for the present model the pressure spectrum slope is correct, in the MRT case the slope of the pressure is closer to $-5/3$ (see Fig. 18). This difference indicates that our new model represents the dynamics of the flow with a much greater accuracy.

5 Conclusion

In this paper we demonstrated the existence of a recursive formula that allows the reconstruction of the non-equilibrium moments of the Boltzmann-BGK equation at any order, only by knowing the lower order moments. This property allows to propose a regularization procedure for the BGK lattice Boltzmann method that is increasing the overall accuracy of the method and removing the majority of the visible spurious modes present in standard BGK and MRT models. This is shown by two benchmarks: the wall–dipole interaction (2D case)

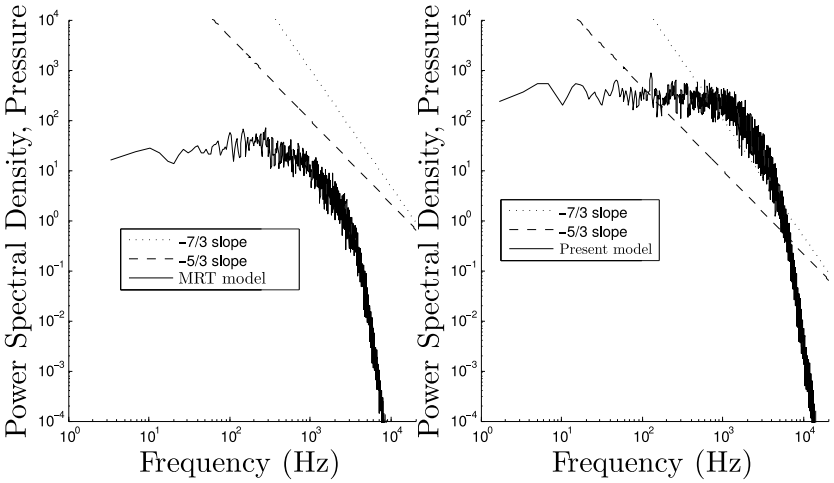

Figure 18: Pressure power spectrum with respect to the frequency for the MRT model (left) and the present model (right).

and the turbulent jet (3D case). Although in the 2D case the increase in accuracy of the model is not spectacular, the stability is greatly improved. For the 3D case a great improvement is shown. Not only the Reynolds stresses are found to be more accurately represented (with respect to the MRT model) but the pressure spectrum has the expected behavior.

Finally one can notice that the model acts like an implicit large eddy simulation model, since the turbulent behavior of the jet is reproduced accurately without any need to use an explicit turbulence model. Its relative simplicity and low cost of implementation make it very appealing for high Reynolds number and moderately high Mach numbers (of a maximal value of roughly 0.5).

An interesting optimization of the present scheme could be achieved by using a D3Q19/D3Q15 quadrature instead of the D3Q27 used here. To do so the recursive formula used throughout this paper should be generalized to alternative basis vectors that are not Hermite polynomials.

Finally the present approach may also be extensible for higher order quadratures (and higher order physics where one includes temperature for example) like thermal and compressible flows where one could reduce dramatically the memory needs of such cases (which is excessive for the moment since one needs D3Q121 quadratures). It could also provide a way to deal with boundary conditions for these kind of models, since with a very limited amount of information, one can reconstruct the complete populations with an accuracy consistent with the model.

Acknowledgments

I would like to acknowledge Pierre Sagaut, Bastien Chopard, Jonas Latt, Federico Brogi, and Christophe Coreixas for the enlightening discussions and also Andreas Malaspinas for a critical proof-reading. I would like to thankfully acknowledge the support of the Swiss National Science Foundation SNF (Award

PA00P2_145364).

A Computation of the recursive relation for off-equilibrium Hermite coefficients

The aim of this section is to prove Eq. (31) that we recall here

$$a^{(n)}_{1,\alpha_1...\alpha_n} = a^{(n-1)}_{1,\alpha_1...\alpha_{n-1}} u_{\alpha_n} + \left(u_{\alpha_1}...u_{\alpha_{n-2}} a^{(2)}_{1,\alpha_{n-1}\alpha_n} + \text{perm}(\alpha_n) \right).$$

To prove it we need three relations. The first is the recursive relation of the equilibrium distribution Hermite coefficients (see Shan et al. [2006], Malaspinas [2009])

$$a^{(n)}_{0,\alpha_1,...,\alpha_n} = a^{(n-1)}_{0,\alpha_1,...,\alpha_{n-1}} u_{\alpha_n}, \text{ and } a^{(0)}_0 = \rho. \tag{79}$$

The second is that the order zero Chapman–Enskog expansion of the continuous Boltzmann–BGK equation leads to the Euler equations

$$\partial_t \rho + \boldsymbol{\nabla} \cdot (\rho \boldsymbol{u}) = 0, \tag{80}$$

$$\rho \partial_t \boldsymbol{u} + \rho \boldsymbol{u} \cdot \boldsymbol{\nabla} \boldsymbol{u} = -\boldsymbol{\nabla} \rho. \tag{81}$$

And finally the order one Chapman–Enskog expansion of the Hermite coefficients

$$\begin{aligned} -\frac{1}{\tau} a^{(n)}_{1,\alpha_1,...,\alpha_n} = {} & \partial_t a^{(n)}_{0,\alpha_1,...,\alpha_n} + \partial_{\alpha_{n+1}} a^{(n+1)}_{0,\alpha_1,...,\alpha_{n+1}} \\ & + \left(\partial_{\alpha_1} a^{(n-1)}_{0,\alpha_2,...,\alpha_n} + \text{perm} \right), \end{aligned} \tag{82}$$

where "perm" stands for all the cyclic permutation of indexes $\alpha_1, ..., \alpha_{n-1}$.

Replacing n by $n-1$ in this last equation and multiplying the result by u_α one gets

$$\begin{aligned} -\frac{1}{\tau} u_{\alpha_n} a^{(n-1)}_{1,\alpha_1,...,\alpha_{n-1}} = {} & u_{\alpha_n} \partial_t a^{(n-1)}_{0,\alpha_1,...,\alpha_{n-1}} + u_{\alpha_n} \partial_{\alpha_{n+1}} a^{(n)}_{0,\alpha_1,...,\alpha_{n-1},\alpha_{n+1}} \\ & + u_{\alpha_n} \left(\partial_{\alpha_1} a^{(n-2)}_{0,\alpha_2,...,\alpha_{n-2}} + \text{perm} \right). \end{aligned} \tag{83}$$

Using the chain rule one can rewrite this equation as

$$\begin{aligned} -\frac{1}{\tau} u_{\alpha_n} a^{(n-1)}_{1,\alpha_1,...,\alpha_{n-1}} = {} & \underbrace{\partial_t a^{(n)}_{0,\alpha_1,...,\alpha_n} + \partial_{\alpha_{n+1}} a^{(n+1)}_{0,\alpha_1,...,\alpha_{n+1}} + \left(\partial_{\alpha_1} a^{(n-1)}_{0,\alpha_2,...,\alpha_n} + \text{perm} \right)}_{(i)} \\ & \underbrace{- a^{(n-1)}_{0,\alpha_1,...,\alpha_{n-1}} \partial_t u_{\alpha_n} - a^{(n)}_{0,\alpha_1,...,\alpha_{n-1},\alpha_{n+1}} \partial_{\alpha_{n+1}} u_{\alpha_n}}_{(ii)} \\ & \underbrace{- \partial_{\alpha_n} a^{(n-1)}_{0,\alpha_1,...,\alpha_{n-1}} - \left(a^{(n-2)}_{0,\alpha_2,...,\alpha_{n-2}} \partial_{\alpha_1} u_{\alpha_n} + \text{perm}(\alpha_n) \right)}_{(iii)}, \end{aligned} \tag{84}$$

where $\text{perm}(\alpha_n)$ is the cyclic permutation of all the indexes not equal to α_n (the α_n index never changes position). The (i) part of the above equation is equal to (see Eq. (82))

$$(i) = -\frac{1}{\tau} a^{(n)}_{1,\alpha_1,...,\alpha_n}. \tag{85}$$

The (ii) can be rewritten

$$\begin{aligned}(ii) &= -a^{(n-1)}_{0,\alpha_1,\ldots,\alpha_{n-1}}\left(\partial_t u_{\alpha_n} + u_{\alpha_{n+1}}\partial_{\alpha_{n+1}} u_{\alpha_n}\right)\\ &= u_{\alpha_1}\cdots u_{\alpha_{n-1}}\partial_{\alpha_n}\rho,\end{aligned} \tag{86}$$

where in the first equation we used Eq. (79) and in the second we used Eq. (81). Finally the (iii) part reads

$$\begin{aligned}(iii) &= -2\left(a^{(n-2)}_{0,\alpha_1,\ldots,\alpha_{n-2}} S_{\alpha_{n-1}\alpha_n} + \mathrm{perm}(\alpha_n)\right) - u_{\alpha_1}\cdots u_{\alpha_{n-1}}\partial_{\alpha_n}\rho,\\ &= \frac{1}{\rho\tau}\left(a^{(n-2)}_{0,\alpha_1,\ldots,\alpha_{n-2}} a^{(2)}_{1,\alpha_{n-1}\alpha_n} + \mathrm{perm}(\alpha_n)\right) - u_{\alpha_1}\cdots u_{\alpha_{n-1}}\partial_{\alpha_n}\rho,\end{aligned} \tag{87}$$

where we used the chain rule in the first equation and Eq. (25) in the second equation.

Finally adding (i), (ii), and (iii) one obtains

$$a^{(n)}_{1,\alpha_1\ldots\alpha_n} = a^{(n-1)}_{1,\alpha_1\ldots\alpha_{n-1}} u_{\alpha_n} + \left(u_{\alpha_1}\ldots u_{\alpha_{n-2}} a^{(2)}_{1,\alpha_{n-1}\alpha_n} + \mathrm{perm}(\alpha_n)\right).$$

B The higher order off-equilibrium Hermite coefficients and implementation formulas

In two dimensions the off-equilibrium Hermite coefficients $\boldsymbol{a}^{(n)}_1$ are given by

$$a^{(3)}_{1,xyy} = u_x a^{(2)}_{1,yy} + 2u_y a^{(2)}_{1,xy} + \underbrace{\tau\rho u_y^3\partial_y u_x}_{*}, \tag{88}$$

$$a^{(3)}_{1,xxy} = 2u_x a^{(2)}_{1,xy} + u_y a^{(2)}_{1,xx} + \underbrace{\tau\rho u_x^3\partial_x u_y}_{*}, \tag{89}$$

$$a^{(4)}_{1,xxyy} = u_y a^{(3)}_{xxy} + u_x^2 a^{(2)}_{1,yy} + 2u_x u_y a^{(2)}_{1,xy} + \underbrace{\tau\rho u_x u_y\left(u_x^2\partial_x u_y + u_y^2\partial_y u_x\right)}_{*}. \tag{90}$$

In three dimensions the off-equilibrium coefficients at order $n = 3$ read

$$a^{(3)}_{1,xxy} = 2u_x a^{(2)}_{1,xy} + u_y a^{(2)}_{1,xx} + \underbrace{\tau\rho u_x^3\partial_x u_y}_{*}, \tag{91}$$

$$a^{(3)}_{1,xxz} = 2u_x a^{(2)}_{1,xz} + u_z a^{(2)}_{1,xx} + \underbrace{\tau\rho u_x^3\partial_x u_z}_{*}, \tag{92}$$

$$a^{(3)}_{1,xyy} = u_x a^{(2)}_{1,yy} + 2u_y a^{(2)}_{1,xy} + \underbrace{\tau\rho u_y^3\partial_y u_x}_{*}, \tag{93}$$

$$a^{(3)}_{1,xzz} = u_x a^{(2)}_{1,zz} + 2u_z a^{(2)}_{1,xz} + \underbrace{\tau\rho u_z^3\partial_z u_x}_{*}, \tag{94}$$

$$a^{(3)}_{1,yzz} = u_y a^{(2)}_{1,zz} + 2u_z a^{(2)}_{1,yz} + \underbrace{\tau\rho u_z^3\partial_z u_y}_{*}, \tag{95}$$

$$a^{(3)}_{1,yyz} = 2u_y a^{(2)}_{1,yz} + u_z a^{(2)}_{1,yy} + \underbrace{\tau\rho u_y^3\partial_y u_z}_{*}, \tag{96}$$

$$a^{(3)}_{1,xyz} = u_x a^{(2)}_{1,yz} + u_y a^{(2)}_{1,xz} + u_z a^{(2)}_{1,xy}, \tag{97}$$

while the $n = 4$ are given by

$$a^{(4)}_{1,xxyy} = u_x^2 a^{(2)}_{1,yy} + 2u_x u_y a^{(2)}_{1,xy} + u_y a^{(3)}_{1,xxy} + \underbrace{\rho\tau u_x u_y \left(2u_y^2 \partial_y u_x + u_x^2 \partial_x u_y\right)}_{*}, \tag{98}$$

$$a^{(4)}_{1,xxzz} = u_x^2 a^{(2)}_{1,zz} + 2u_x u_z a^{(2)}_{1,xz} + u_z a^{(3)}_{1,xxz} + \underbrace{\rho\tau u_x u_z \left(u_x^2 \partial_x u_z + 2u_z^2 \partial_z u_x\right)}_{*}, \tag{99}$$

$$a^{(4)}_{1,yyzz} = u_y^2 a^{(2)}_{1,zz} + 2u_y u_z a^{(2)}_{1,yz} + u_z a^{(3)}_{1,yyz} + \underbrace{\rho\tau u_y u_z \left(u_y^2 \partial_y u_z + 2u_z^2 \partial_z u_y\right)}_{*}, \tag{100}$$

$$a^{(4)}_{1,xyzz} = u_x u_y a^{(2)}_{1,zz} + u_x u_z a^{(2)}_{1,yz} + u_y u_z a^{(2)}_{1,xz} + u_z a^{(3)}_{1,xyz} + \underbrace{\rho\tau u_z^3 \left(u_x \partial_z u_y + u_y \partial_z u_x\right)}_{*}, \tag{101}$$

$$a^{(4)}_{1,xyyz} = 2u_x u_y a^{(2)}_{1,yz} + u_y^2 a^{(2)}_{1,xz} + u_z a^{(3)}_{1,xyy} + \underbrace{\rho\tau u_x u_y^3 \partial_y u_z}_{*}, \tag{102}$$

$$a^{(4)}_{1,xxyz} = u_x^2 a^{(2)}_{1,yz} + 2u_x u_y a^{(2)}_{1,xz} + u_z a^{(3)}_{1,xxy} + \underbrace{\rho\tau u_y u_x^3 \partial_x u_z}_{*}. \tag{103}$$

while the $n = 5$ and $n = 6$ are are found to be

$$a^{(5)}_{1,xxyzz} = u_x^2 u_y a^{(2)}_{1,zz} + u_x^2 u_z a^{(2)}_{1,yz} + 2u_x u_y u_z a^{(2)}_{1,xz} + u_z a^{(4)}_{1,xxyz} + \underbrace{\rho\tau u_x u_z \left(u_x^2 u_y \partial_x u_z + 2u_y u_z^2 \partial_z u_x + u_x u_z^2 \partial_z u_y\right)}_{*}, \tag{104}$$

$$a^{(5)}_{1,xxyyz} = 2u_x^2 u_y a^{(2)}_{1,yz} + 2u_x u_y^2 a^{(2)}_{1,xz} + u_z a^{(4)}_{1,xxyy} + \underbrace{\rho\tau u_x^2 u_y^2 \left(u_x \partial_x u_z + u_y \partial_y u_z\right)}_{*}, \tag{105}$$

$$a^{(5)}_{1,xyyzz} = u_x u_y^2 a^{(2)}_{1,zz} + 2u_x u_y u_z a^{(2)}_{1,yz} + u_y^2 u_z a^{(2)}_{1,xz} + u_z a^{(4)}_{1,xyyz} + \underbrace{\rho\tau u_y u_z \left(u_y u_z^2 \partial_z u_x + u_x u_y^2 \partial_y u_z + 2u_x u_z^2 \partial_z u_y\right)}_{*}, \tag{106}$$

$$a^{(6)}_{1,xxyyzz} = u_x^2 u_y^2 a^{(2)}_{1,zz} + 2u_x^2 u_y u_z a^{(2)}_{1,yz} + 2u_x u_y^2 u_z a^{(2)}_{1,xz} + u_z a^{(5)}_{1,xxyyz} + \underbrace{\rho\tau u_x u_y u_z \left(u_x^2 u_y \partial_x u_z + 2u_y u_z^2 \partial_z u_x + u_x u_y^2 \partial_y u_z + 2u_x u_z^2 \partial_z u_y\right)}_{*}. \tag{107}$$

The $*$ terms are the ones that are not present in the continuous case (see Eq. (31)) and are due to the discretization of the microscopic velocity space. One can see that as pointed out in Subsec. 3.3 these terms are of order $\emptyset(\mathrm{Ma}^{n+1})$ for the coefficients of order n, which makes them one order of magnitude smaller

than the other composing them. Therefore they are simply ignored for the computation of the $\boldsymbol{a}_1^{(n)}$ terms.

References

S. Ansumali and I. V. Karlin. Single relaxation time model for entropic lattice Boltzmann methods. *Phys. Rev. E*, 65(5):056312, May 2002. doi: 10.1103/PhysRevE.65.056312.

P. L. Bhatnagar, E. P. Gross, and M. Krook. A Model for Collision Processes in Gases. I. Small Amplitude Processes in Charged and Neutral One-Component Systems. *Phys. Rev.*, 94(3):511–525, May 1954. doi: 10.1103/PhysRev.94.511.

C. Bogey, C. Bailly, and D. Juvé. Noise investigation of a high subsonic, moderate reynolds number jet using a compressible large eddy simulation. *Theoretical and Computational Fluid Dynamics*, 16(4):273–297, 2003. doi: 10.1007/s00162-002-0079-4.

B. M. Boghosian, P. J. Love, P. V. Coveney, I. V. Karlin, S. Succi, and J. Yepez. Galilean-invariant lattice-Boltzmann models with H theorem. *Phys. Rev. E*, 68(2):025103, Aug 2003. doi: 10.1103/PhysRevE.68.025103.

S. Chapman and T. G. Cowling. *The mathematical theory of nonuniform gases.* Cambridge University Press, Cambridge, 1960.

S. S. Chikatamarla, S. Ansumali, and I. V. Karlin. Entropic lattice Boltzmann models for hydrodynamics in three dimensions. *Phys. Rev. Lett.*, 97(1): 010201, 2006. doi: 10.1103/PhysRevLett.97.010201.

H. J. H. Clercx and C.-H. Bruneau. The normal and oblique collision of a dipole with a no-slip boundary. *Comput. Fluids*, 35:245–279, 2006.

P. J. Dellar. Bulk and shear viscosities in lattice Boltzmann equations. *Phys. Rev. E*, 64(3):031203, Aug 2001. doi: 10.1103/PhysRevE.64.031203.

P. J. Dellar. Incompressible limits of lattice Boltzmann equations using multiple relaxation times. *J. Comp. Phys.*, 190:351–370, 2003.

D. d'Humières. Generalized lattice-Boltzmann equations. *Progress in Astronautics and Aeronautics*, 159:450–458, 1992.

D. d'Humières, I. Ginzburg, M. Krafczyk, P. Lallemand, and L.-S.Luo. Multiple-relaxation-time lattice Boltzmann models in three dimensions. *Phil. Trans. R. Soc. A*, 360:437–451, 2002.

W. K. George, P. D. Beuther, and R. EA. Arndt. Pressure spectra in turbulent free shear flows. *J. Fluid Mech.*, 148:155–191, 1984.

H. Grad. Note on the N-dimensional Hermite polynomials. *Commun. Pure Appl. Maths*, 9:325, 1949a.

H. Grad. On the kinetic theory of rarefied gases. *Commun. Pure Appl. Maths*, 9:331, 1949b.

K. Huang. *Statistical Mechanics*. J. Wiley, New York, 1987.

T. Inamuro, M. Yoshina, and F. Ogino. A non-slip boundary condition for lattice Boltzmann simulations. *Phys. Fluids*, 7:2928–2930, 1995.

M. Krafczyk, J. Tölke, and L.-S. Luo. Large-eddy simulations with a multiple-relaxation-time LBE model. *Int. J. Mod. Phys. B*, 17:33–39, 2003. doi: 10.1142/S0217979203017059.

Pierre Lallemand and Li-Shi Luo. Theory of the lattice boltzmann method: Dispersion, dissipation, isotropy, galilean invariance, and stability. *Phys. Rev. E*, 61:6546–6562, Jun 2000. doi: 10.1103/PhysRevE.61.6546.

J. Latt. *Hydrodynamic limit of lattice Boltzmann equations*. PhD dissertation, University of Geneva, Geneva, Switzerland, 2007. URL `http://www.unige.ch/cyberdocuments/theses2007/LattJ/meta.html`.

J. Latt and B. Chopard. Lattice Boltzmann method with regularized non-equilibrium distribution functions. *Math. Comp. Sim.*, 72:165–168, 2006.

J. Latt and B. Chopard. A benchmark case for lattice Boltzmann: turbulent dipole-wall collision. *Int. J. Mod. Phys. C*, 18:619–626, 2007.

J. Latt, B. Chopard, O. Malaspinas, M. Deville, and A. Michler. Straight velocity boundaries in the lattice Boltzmann method. *Phys. Rev. E*, 77(5): 056703–+, May 2008. doi: 10.1103/PhysRevE.77.056703.

O. Malaspinas. *Lattice Boltzmann method for the simulation of viscoelastic fluid flows*. PhD dissertation, EPFL, Lausanne, Switzerland, 2009. URL `http://library.epfl.ch/theses/?nr=4505`.

O. Malaspinas and P. Sagaut. Consistent subgrid scale modelling for lattice Boltzmann methods. *J. Fluid. Mech.*, 700:514–542, JUN 10 2012. ISSN 0022-1120. doi: {10.1017/jfm.2012.155}.

O. Malaspinas, M. Deville, and B. Chopard. Towards a physical interpretation of the entropic lattice Boltzmann method. *Phys. Rev. E*, 78:066705, Dec 2008. doi: 10.1103/PhysRevE.78.066705. URL `http://link.aps.org/doi/10.1103/PhysRevE.78.066705`.

O. Malaspinas, B. Chopard, and J. Latt. General regularized boundary condition for multi-speed lattice Boltzmann models. *Comp. Fluids*, 49(1):29–35, OCT 2011. doi: {10.1016/j.compfluid.2011.04.010}.

S. B. Pope. *Turbulent Flows*. Cambridge University Press, Cambridge, 2005.

D. Ricot, S. Marié, P. Sagaut, and C. Bailly. Lattice Boltzmann method with selective viscosity filter. *J. Comp. Phys.*, 228(12):4478–4490, 2009. ISSN 0021-9991. doi: DOI:10.1016/j.jcp.2009.03.030.

X. Shan, X.-F. Yuan, and H. Chen. Kinetic theory representation of hydrodynamics: a way beyond the Navier-Stokes equation. *J. Fluid Mech.*, 550: 413–441, 2006. doi: 10.1017/S0022112005008153.

P. A. Skordos. Initial and boundary conditions for the lattice Boltzmann method. *Phys. Rev. E*, 48:4823–4842, 1993.

H. Xu and P. Sagaut. Optimal low-dispersion low-dissipation LBM schemes for computational aeroacoustics. *J. Comp. Phys.*, 230(13):5353 – 5382, 2011. ISSN 0021-9991. doi: http://dx.doi.org/10.1016/j.jcp.2011.03.040.

H. Xu and P. Sagaut. Analysis of the absorbing layers for the weakly-compressible lattice boltzmann methods. *J. Comp. Phys.*, 245(0):14 – 42, 2013. ISSN 0021-9991. doi: http://dx.doi.org/10.1016/j.jcp.2013.02.051.

H. Xu, O. Malaspinas, and P. Sagaut. Sensitivity analysis and determination of free relaxation parameters for the weakly-compressible mrt–lbm schemes. *J. Comp. Phys.*, 231(21):7335 – 7367, 2012. ISSN 0021-9991. doi: http://dx.doi.org/10.1016/j.jcp.2012.07.005.

Raoyang Zhang, Xiaowen Shan, and Hudong Chen. Efficient kinetic method for fluid simulation beyond the navier-stokes equation. *Phys. Rev. E*, 74:046703, Oct 2006. doi: 10.1103/PhysRevE.74.046703. URL `http://link.aps.org/doi/10.1103/PhysRevE.74.046703`.

Q. Zou and X. He. On pressure and velocity boundary conditions for the lattice Boltzmann BGK model. *Phys. Fluids*, 9:1592–1598, 1997.